Volume 4
Number 1
January 2026
Pages 1–240

EES Catalysis

rsc.li/EESCatalysis

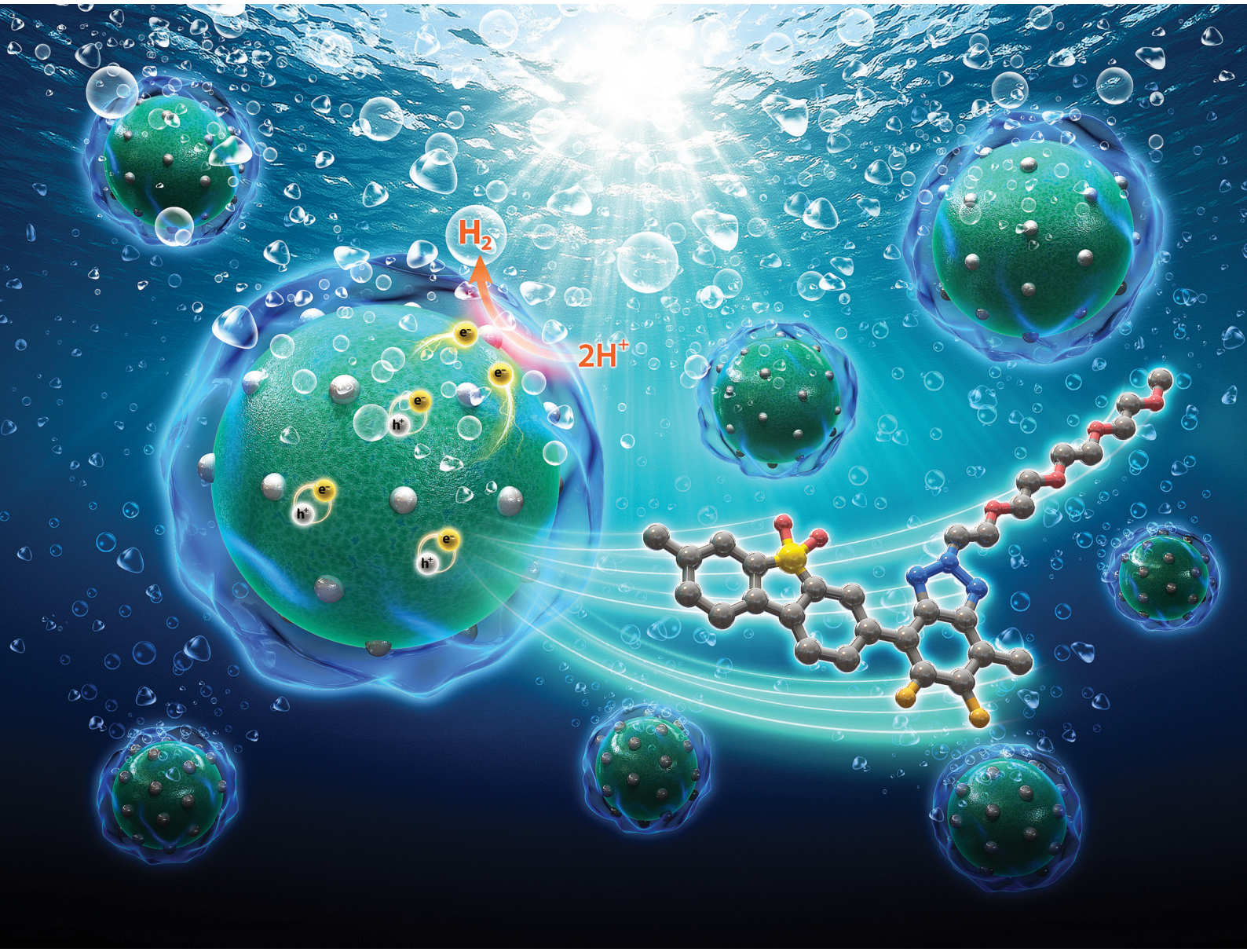

ISSN 2753-801X

ROYAL SOCIETY OF CHEMISTRY

PAPER
Jihoon Lee, Hyojung Cha *et al.*
Synergistic dual-electron acceptors in linear conjugated polymers for boosting photocatalytic hydrogen evolution

EES Catalysis

PAPER

View Article Online
View Journal | View Issue

Check for updates

Cite this: *EES Catal.*, 2026, 4, 86

Synergistic dual-electron acceptors in linear conjugated polymers for boosting photocatalytic hydrogen evolution

Sowon Kim,†[a] Youngwoong Yu,†[b] Hyunwoo Choi,[b] Gayoung Ham,[a] Sanghyeok An,[c] Soyeon Lee,[d] Jiwoong Yang,[d] Dae Sung Chung,[c] Jihoon Lee *[b] and Hyojung Cha *[a]

Received 23rd May 2025,
Accepted 6th August 2025

DOI: 10.1039/d5ey00155b

rsc.li/eescatalysis

A conjugated polymer photocatalyst containing dual-electron acceptor units, dibenzo[*b*,*d*]thiophene sulfone (DBS) and 2,1,3-benzothiadiazole (BT), known as **PBT**, has been synthesized for its strong electron-withdrawing abilities and structural flexibility. However, the inherent hydrophobicity of **PBT** leads to significant particle aggregation, hindering colloidal stability and electron transfer to protons. To overcome these limitations, fluorine and ethylene glycol (EG) groups are strategically incorporated into the BT unit to enhance molecular planarity and hydrophilicity, respectively. This molecular engineering effectively suppresses exciton and charge recombination, facilitating efficient charge separation and extraction. Comprehensive spectroscopic analyses—including time-resolved photoluminescence (Tr-PL) and transient absorption spectroscopy (TAS)—reveal that EG-functionalized polymers exhibit prolonged exciton lifetimes and strong photoinduced absorption at early timescales, indicating both suppressed non-radiative recombination and effective charge generation. Importantly, these modifications enable rapid charge separation and transfer with more efficient electron extraction to protons, mitigating charge accumulation within aggregated domains. Among the modified polymers, **4EG-PBTz-F**, with di-fluoro substituents and tetra-ethylene glycol groups, achieves the highest hydrogen evolution rates of 15.476 mmol g^{-1} and 3.095 mmol g^{-1} h^{-1} with a 3 wt% Pt co-catalyst. These results highlight the effectiveness of dual-electron acceptor design and interfacial control, offering a multi-faceted design strategy in photocatalytic hydrogen evolution systems.

Broader context

Hydrogen is a promising clean energy carrier in the transition to a sustainable energy economy, particularly when generated from sunlight *via* photocatalytic water splitting. As a direct solar-to-chemical energy conversion strategy, photocatalysis offers a simple and scalable route for hydrogen production without reliance on external electrical input or complex device architectures. Organic photocatalysts provide unique advantages in this context, including molecular tunability, low-temperature processability, and compatibility with aqueous systems. Their structural flexibility allows for precise modulation of light absorption, exciton behavior, and interfacial charge transfer dynamics, offering a powerful platform for material innovation in solar fuel generation. In this study, we report a dual-electron acceptor-based linear conjugated polymer system, rationally designed with fluorinated and ethylene glycol-functionalized side chains. This design enhances exciton stability, promotes rapid charge separation, and facilitates strong polymer–solvent interactions, resulting in significantly improved hydrogen evolution activity. By leveraging the molecular design freedom of organic materials, this work contributes to the development of efficient photocatalysts for solar-driven hydrogen production. These findings highlight the broader potential of organic systems in advancing decentralized, carbon-neutral energy technologies.

[a] *School of Energy Engineering, Kyungpook National University, Daehak-ro 80, Buk-gu, Daegu, 41566, Republic of Korea. E-mail: hcha@knu.ac.kr*
[b] *Department of Polymer Science and Engineering & Department of IT·Energy, Convergence (BK21 Four), Korea National University of Transportation (KNUT), Chungju, 27469, Republic of Korea. E-mail: jihoonli@ut.ac.kr*
[c] *Department of Chemical Engineering, Pohang University of Science and Technology (POSTECH), Pohang, 37673, Republic of Korea*
[d] *Department of Energy Science and Engineering, Daegu Gyeongbuk Institute of Science and Technology (DGIST), Daegu, 42988, Republic of Korea*
† Both authors contributed equally.

Introduction

Hydrogen consumption is increasing as industries adopt eco-friendly energy in response to climate change, with green hydrogen derived from renewable sources such as solar, wind, and bioenergy.[1,2] Solar-driven photocatalytic water-splitting, a process that utilizes sunlight to separate water into hydrogen

Open Access Article. Published on 07 August 2025. Downloaded on 1/18/2026 3:15:49 PM. This article is licensed under a Creative Commons Attribution-NonCommercial 3.0 Unported Licence.

© 2026 The Author(s). Published by the Royal Society of Chemistry

Open Access Article. Published on 07 August 2025. Downloaded on 1/18/2026 3:15:49 PM. This article is licensed under a Creative Commons Attribution-NonCommercial 3.0 Unported Licence.

and oxygen, not only directly utilizes solar energy but also facilitates hydrogen fuel storage, presenting a promising avenue for integrating renewable energy.[3–7] Extensive research in photocatalysis has primarily focused on inorganic materials, such as metal oxides and chalcogenides.[8–12] Although these materials exhibit high stability and efficient electron mobility due to their well-ordered crystalline structure, they face significant limitations stemming from their wide bandgaps, which confine light absorption to the UV region, and challenges in engineering molecular structures due to rigid structural frameworks. To address these challenges, recent studies have shifted toward conjugated organic molecules, including carbon nitrides, covalent organic frameworks, and linear conjugated polymers (LCPs). These materials offer distinct advantages such as cost-effectiveness, enhanced light absorption efficiency, and tunable molecular structures, making them promising candidates for photocatalytic applications in hydrogen evolution.[13–19]

In particular, LCPs are gaining attention due to efficient charge transport facilitated by their π–π stacking structure and their versatility for processing into films and particles suspended in solutions, as well as low environmental impact.[20–24] Among these materials, dibenzo[*b*,*d*]thiophene sulfone (DBS) has recently emerged as an effective organic photocatalytic moiety in current research.[16,18] DBS is an electron acceptor that is known to offer a water-compatible environment around its polar sulfone unit, promoting the electron transfer necessary for proton reduction.[25] However, DBS synthesized as a single repeating unit for a homopolymer, referred to as P10, forms sub-micrometer-scale particles with limited uniformity. This affects dispersion stability and imparts a rigid structure that limits side-chain engineering.[18] Consequently, electron donor–acceptor (D–A) copolymers combining electron donor moieties with DBS have been explored to overcome these limitations, although the reduced proportion of the acceptor unit in these copolymers can decrease the overall electron-withdrawing ability.[26,27] To further enhance the photocatalytic efficiency, recent studies have investigated dual-acceptor systems incorporating sulfone-based groups, which increase the electron output sites and improve charge separation and transfer efficiency.[28]

Building upon this strategy, this study introduces a 2,1,3-benzothiadiazole (BT) unit as an additional electron acceptor in a DBS-based polymer, resulting in **PBT**, with the aim of achieving both enhanced structural adaptability and proton reduction efficiency (Fig. 1). Recent research indicates that the nitrogen (N) atoms in the BT unit play a central role in photocatalytic activation, particularly in proton reduction reactions.[29] While BT alone has limitations such as poor light absorption and hydrophobic characteristics, integrating it with DBS could mitigate these drawbacks.

In this study, a dual-acceptor polymer, **PBT**, was synthesized with enhanced electron-accepting ability. Fluorine (F) substituents and ethylene glycol (EG) side chains were introduced to the aromatic carbons and diazole ring of the BT unit, respectively, to enhance backbone planarity *via* hydrogen bonding and to enhance polymer–solvent interactions in hydrophilic environments.[30–32] These structural modifications are expected to increase the dispersibility of LCPs, facilitating efficient charge separation and transfer, ultimately impacting photocatalytic activity. Density functional theory (DFT) calculations and optical property analyses were performed to investigate how the bonding characteristics and charge density distribution of the **PBT**-based polymer affect exciton generation and recombination across the absorption region. Charge carrier dynamics were measured to trace the behavior of electron–hole pairs over time, analyzing mechanisms of charge separation and transfer. Furthermore, morphological properties and hydrophilicity were evaluated to assess polymer–solvent interactions resulting from side-chain engineering, providing insights into the dispersibility and stability of the photocatalyst. Consequently, **4EG-PBTz-F**, incorporating di-fluoro substituents and tetra-ethylene glycol, exhibited a high hydrogen evolution rate (HER) of 3.095 mmol g^{-1} h^{-1} with a 3 wt% Pt co-catalyst under 1 sun illumination. This molecular design also enabled substantial stability over extended periods.

Results and discussion

Material synthesis and characterization

Here, we designed and synthesized novel monomers and copolymers using three acceptor units for organic photocatalysts in water-splitting hydrogen evolution. The detailed synthetic procedures and characterization are presented in the SI (Schemes S1–S13 and Fig. S1–S23).[33,34] Among the acceptor units, the DBS unit is extensively studied due to its high hydrophilicity, excellent electron-accepting ability, and effective electron transfer properties (Schemes S1 and S2).[53,54] The second is the BT unit, which has recently emerged as a promising acceptor due to its N reduction site (Scheme S3).[39] The last unit is the 5,6-difluoro-2*H*-benzo[*d*][1,2,3]triazole (BTz) unit (Scheme S4). The BTz unit can leverage the advantages of organic materials, particularly its ability to accommodate various substituent modifications on the N site. To enhance both stability and charge mobility, we introduced F as a substituent.[45] Additionally, we incorporated three different lengths of EG-based side chains to improve solubility in water, ultimately developing new monomers (Schemes S5–S7).[46–48] We successfully designed and systematically synthesized three soluble (***n*EG-PBTz-F**s) and three insoluble (**PBT**, **PBT-F**, and **PBTzH-F**) LCPs as photocatalysts by fixing DBS and changing the BT-based monomers (Fig. 1 and Schemes S8–S13). These conjugated polymer photocatalysts were easily polymerized using Suzuki aryl–aryl coupling reaction with $Pd(PPh_3)_4$.[35] End-capping was performed using bromobenzene and phenylboronic acid to block reactive terminal groups that could impact performance. This alternating arrangement and end-capping enhance the reliability of HER characteristic assessments. Moreover, previous studies have indicated that Suzuki aryl–aryl coupling polymerization, which results in residual palladium metal, generally performs better than Yamamoto aryl–aryl coupling polymerization, which leaves residual nickel

Open Access Article. Published on 07 August 2025. Downloaded on 1/18/2026 3:15:49 PM.
This article is licensed under a Creative Commons Attribution-NonCommercial 3.0 Unported Licence.

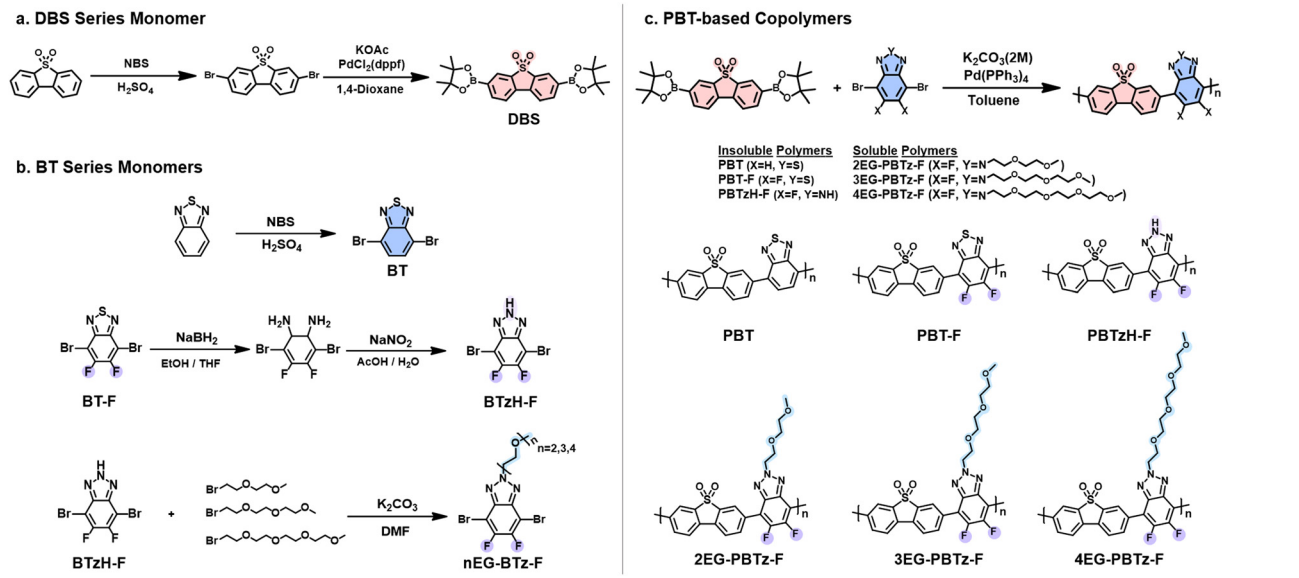

Fig. 1 Schematic illustration of the synthetic routes and chemical structures of (a) DBS series monomers, (b) BT series monomers, and (c) **PBT**-based copolymers.

metal.[31] However, excessive residual Pd can negatively affect performance, and significant variation in residual Pd content among copolymers can make it challenging to compare their properties. To address this, we employed repeated precipitation in methanol. We conducted Soxhlet extraction with various solvents to remove small molecules and oligomers, yielding a high polydispersity index (PDI) and minimizing residual Pd content (Table S1).[45]

We conducted structural analyses of the synthesized LCPs and investigated factors affecting hydrogen evolution efficiency. Insoluble copolymers such as **PBT**, **PBT-F**, and **PBTzH-F** pose challenges for precise analysis due to their insolubility in typical organic solvents such as THF, DMF and chloroform.[36] To address this limitation, we utilized FT-IR spectroscopy and solid-state ^{13}C cross-polarization magic angle spinning (CP/MAS) nuclear magnetic resonance (NMR) spectroscopy measurements to examine the structures of these insoluble copolymers (Fig. S24). The FT-IR spectra exhibited characteristic peaks at approximately 1600 and 1465 cm^{-1}, corresponding to the typical C=C stretching vibrations of aromatic backbones (Fig. S24a). Furthermore, the C=N stretching vibration from the BT unit was observed at approximately 1650 cm^{-1}. Peaks at approximately 1307 and 1157 cm^{-1} are attributed to the stretching vibrations of the sulfone group (O=S=O) from the DBS unit.[51–54] To further analyze the structure, solid-state ^{13}C CP/MAS NMR spectroscopy was employed for characterization (Fig. S24b). The main peaks ranged from 122 to 136 ppm, with peaks between 122 and 131 ppm attributed to aromatic carbons (C=C, C–H, C–F) in the BT group and aromatic carbons (C=C, C–H) in DBS. In addition, the peak at 136 ppm corresponded to the sulfone group carbons in DBS, while peaks between 149 and 160 ppm were assigned to the C=N bonds in the BT group.[30,39,40]

The soluble polymers (***n*EG-PBTz-F**s) were structurally easier to analyze, and structural analysis was performed using ^{1}H-NMR (400 MHz) spectroscopy. The DBS unit exhibited a characteristic aromatic 6H signal in the range of 8.5–7.5 ppm, while the protons from the EG-based side chains appeared between 5.2 and 3.2 ppm (Fig. S21–S23). Additionally, the molecular weights of the three insoluble polymers could not be determined due to their limited solubility.[37,38] However, the molecular weights of the three soluble polymers were successfully measured using gel permeation chromatography (GPC) with chloroform as the eluent. The GPC results revealed

Table 1 Molecular weight, and optical and electrochemical properties of **PBT**, **PBT-F**, **PBTzH-F**, **2EG-PBTz-F**, **3EG-PBTz-F**, and **4EG-PBTz-F**

Material	M_n/M_w[a] (kDa)	PDI[a]	LUMO[b] (eV)	HOMO[b] (eV)	$E_{g,DFT}$[b] (eV)	$E_{g,opt}$[c] (eV)	λ_{max} (nm)
PBT	—	—	3.02	6.00	2.98	2.98	321/432
PBT-F	—	—	3.10	6.18	3.07	2.66	324/374
PBTzH-F	—	—	2.80	5.99	3.19	2.79	404
2EG-PBTz-F	59.7/71.3	1.19	2.70	5.89	3.19	2.97	369
3EG-PBTz-F	68.6/88.2	1.28	2.70	5.89	3.19	3.00	371
4EG-PBTz-F	71.8/99.3	1.38	2.70	5.89	3.19	2.94	379

[a] Measured by GPC; the eluent was chloroform. [b] Values were calculated *via* DFT calculation. [c] Values were evaluated using a Tauc plot (Fig. S31).

© 2026 The Author(s). Published by the Royal Society of Chemistry

Open Access Article. Published on 07 August 2025. Downloaded on 1/18/2026 3:15:49 PM. This article is licensed under a Creative Commons Attribution-NonCommercial 3.0 Unported Licence.

molecular weights of 59.7 kDa for **2EG-PBTz-F** (PDI = 1.19), 68.6 kDa for **3EG-PBTz-F** (PDI = 1.28), and 71.8 kDa for **4EG-PBTz-F** (PDI = 1.38) (Table 1).

Furthermore, SEM-EDS mapping provided additional structural information, showing uniform distribution of each element across the polymer matrix, which, while not entirely precise, contributed to confirming the structural composition (Fig. S25).[40–42,49] Furthermore, X-ray diffraction (XRD) data indicated that all samples exhibited amorphous characteristics, a common feature in conjugated polymers (Fig. S26a). The introduction of side chains enabled the polymers to become soluble, thereby enhancing their amorphous nature, as evidenced by the broad peaks observed in the XRD patterns of polymers with side chains, indicating a more pronounced amorphous character due to the tendency to disrupt a long-range order. In contrast, polymers without side chains exhibited relatively narrower peaks, suggesting a slight degree of crystallinity. This observation confirms that while side chain introduction enhances the amorphous nature of the polymers, those without side chains may retain some crystalline order.[43–45]

Thermogravimetric analysis (TGA) results revealed that the decomposition temperatures (T_d) of all polymers, whether soluble or insoluble, were close to or exceeded 300 °C, indicating their significant thermal stability (Fig. S26b). The high decomposition threshold implies that the polymers can resist thermal degradation, making them suitable for applications requiring robust thermal endurance.[46,47,50]

The DFT analysis of the polymers, including the distributions of the highest occupied molecular orbital (HOMO) and the lowest unoccupied molecular orbital (LUMO), along with partial charge mapping, provides valuable insights into their potential as photocatalysts for hydrogen evolution (Fig. S27). The spatial separation of the HOMO and LUMO orbitals across the polymer backbones indicates effective charge separation, which is crucial for reducing electron–hole recombination and enhancing photocatalytic efficiency. This separation suggests that the polymers can absorb light energy, facilitating the electron transfer crucial for driving redox reactions in hydrogen evolution. To further assess these theoretical predictions, cyclic voltammetry (CV) measurements were performed for all conjugated polymers (Fig. S28 and Table S2). The electrochemically determined energy levels exhibit general agreement with the theoretical values. These findings support the reliability of DFT calculations in describing the electronic structures of the investigated materials. The partial charge distribution further clarifies the electronic structure, revealing regions of high electron density around the sulfone and nitrogen-containing groups, which are potential active sites for redox reactions. Electron-rich regions favor reduction processes, while electron-deficient regions support oxidation. Moreover, the introduction of side chains, such as EG-based chains, influences the charge distribution, potentially improving electron mobility and supporting charge separation within the polymer matrix. The HOMO–LUMO analysis and partial charge mapping provide a theoretical framework for understanding the electronic and reactive properties of these polymers, thereby aiding in the design and optimization of LCP-based photocatalysts for efficient hydrogen evolution. This combined analysis lays the groundwork for future experimental validation to confirm the predicted photocatalytic performance (Fig. 2 and Fig. S29 and S30).[39–41]

Optical and electronic properties

UV-vis absorption measurements were conducted to investigate the optical properties of the polymers in detail (Fig. 2a). The optical properties measured are summarized in Table 1. The polymer particles for UV-vis spectroscopy were prepared in a triethylamine (TEA):methanol (MeOH):H_2O solution. In the **PBT** structure, the BT unit exhibited an absorption peak at approximately 320 nm, while the DBS unit exhibited a peak at approximately 432 nm.[18] In the case of **PBT-F**, the absorption peak at 374 nm in the UV-vis spectrum is attributed to the DBS unit. This assignment is supported by the disappearance of the 324 nm peak upon the introduction of a nitrogen atom into the BT unit, while the 374 nm peak remains unchanged, indicating that the 324 nm peak corresponds to the BT moiety. Furthermore, the introduction of F substituents increases the electron density around the BT unit, as shown by electrostatic potential (ESP) data, which induces a blue-shift of the DBS-derived absorption peak, resulting in the 374 nm peak observed in **PBT-F**. This redistribution of electron density also decreases both the HOMO and the LUMO energy levels of **PBT-F**, indicating deeper electronic states. Substituting the S atom in BT with an N atom eliminates the BT peak, resulting in a significantly red-shifted absorption peak for DBS. This change is attributed to a more uniform electron density distribution and a decreased dihedral angle, which increases molecular planarity (Fig. S29). The improved planarity facilitates efficient electron transport and reduces peak tailing at lower energies, enhancing the optical properties for photocatalytic applications. In the UV-vis spectrum of **2EG-PBTz-F**, the addition of diethylene glycol side chains to **PBTzH-F** causes a pronounced blue shift of the DBS peak. ESP data confirmed this shift, suggesting that the electron-donating properties of the EG groups localize electrons on the DBS unit backbone. Conversely, the UV spectra of **3EG-PBTz-F** and **4EG-PBTz-F** exhibited a more red-shifted absorption peak compared to **2EG-PBTz-F**. This trend is likely due to the additional EG groups that strengthen hydrogen bonding with water, thereby improving the interaction of polymers with the aqueous environment. These interactions help extend the conjugated system and reduce peak tailing, thereby enhancing light absorption efficiency.

To investigate exciton generation and radiative recombination pathways, we performed photoluminescence (PL) measurements (Fig. 2b). All reaction solutions for the PL measurements were prepared using the polymer in the TEA:MeOH:H_2O solution to maintain consistent UV-vis absorbance. The excitation wavelength was set at 320 nm. The PL intensity for both **PBT** and **PBT-F** is relatively low, likely due to the poor dispersibility of the polymer in the aqueous environment, leading to reduced exciton generation. Notably, **PBT-F** displays split

Open Access Article. Published on 07 August 2025. Downloaded on 1/18/2026 3:15:49 PM.
This article is licensed under a Creative Commons Attribution-NonCommercial 3.0 Unported Licence.

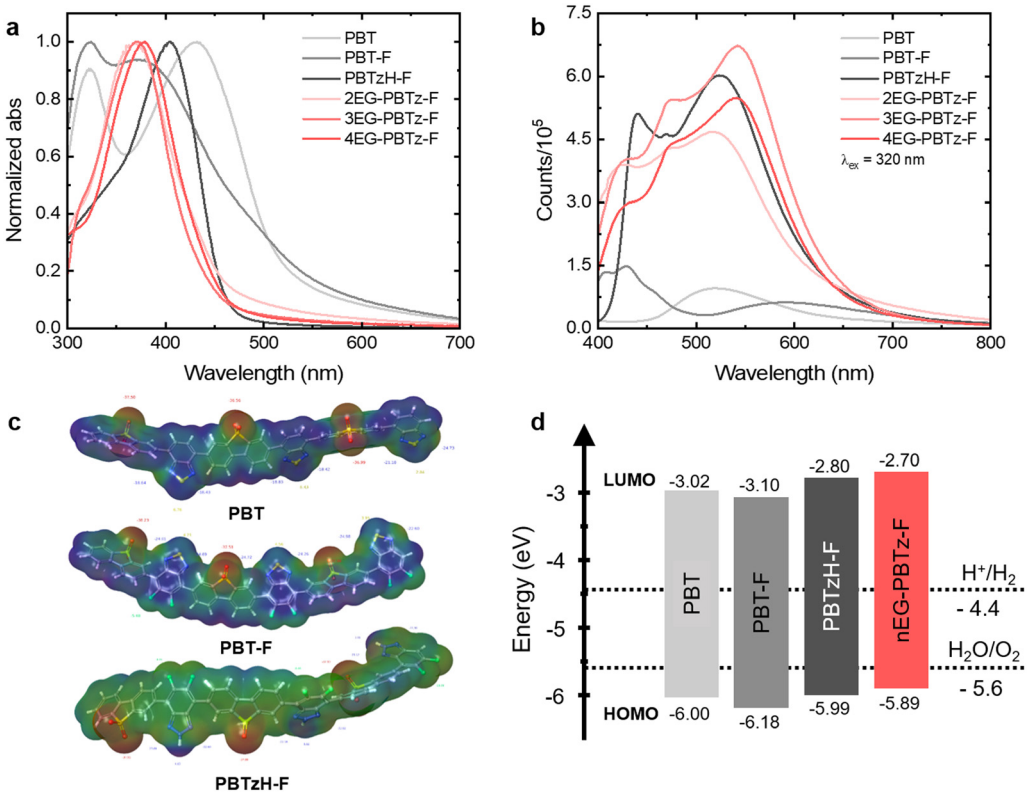

Fig. 2 Measurement of optical properties and electron distribution of the polymer. (a) Normalized UV-vis spectra acquired from polymer particle dispersions prepared in a consistent TEA:MeOH:H_2O solvent ratio. (b) PL spectra of polymer particle dispersions (**PBT**, **PBT-F**, **PBTzH-F**, **2EG-PBTz-F**, **3EG-PBTz-F**, and **4EG-PBTz-F**) measured in a TEA:MeOH:H_2O solvent prepared at the same volume ratio, with excitation at 320 nm for all samples. (c) Electrostatic potential (ESP) data of **PBT**, **PBT-F**, and **PBTzH-F**. The ESP data and energy levels were calculated using DFT calculations. The electron charge density distribution of the ESP is represented by a rainbow color scale, where red indicates regions with a high negative charge, and blue or violet indicates regions with a high positive charge. (d) Schematic energy level diagram of the **PBT**, **PBT-F**, **PBTzH-F**, and ***n*EG-PBTz-F** (*n* = 2, 3, 4) series obtained from DFT simulation.

peaks, indicating that the incorporation of F atoms modifies electron density and facilitates recombination across multiple energy levels. Introducing an N atom into the BT unit enhances electron delocalization, and the enhanced medium interaction improves dispersibility and exciton generation, resulting in a significant increase in the PL intensity. The PL characteristics of polymers containing EG side chains appear similar, possibly due to the convergence of structural and electronic properties upon EG addition. With an increase in the number of EG groups, the PL intensity increases, which can be attributed to the enhanced dispersibility and interactions with the polymer-aqueous environment, which facilitate exciton generation. Notably, **4EG-PBTz-F** exhibits slightly lower PL intensity compared to **3EG-PBTz-F**, likely due to increased non-radiative pathways that facilitate charge separation over radiative recombination. These results highlight the crucial role of side-chain engineering, particularly EG substitution, in enhancing charge transfer dynamics by balancing radiative and non-radiative recombination, ultimately optimizing the photocatalyst for hydrogen evolution.

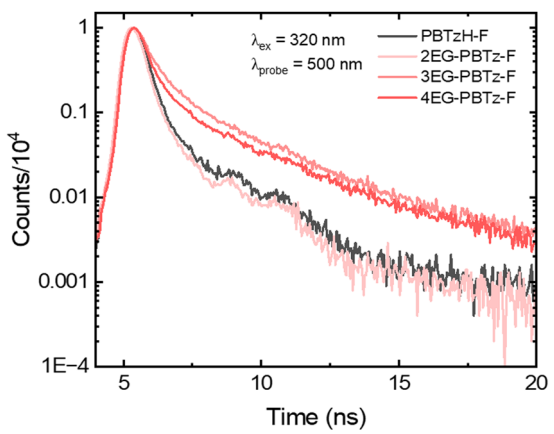

Fig. 3 Time-resolved photoluminescence (Tr-PL) decays of dispersion of polymer particles (**PBTzH-F**, **2EG-PBTz-F**, **3EG-PBTz-F** and **4EG-PBTz-F**). All polymers were dispersed in the same volume ratio of TEA:MeOH:H_2O, excited at 320 nm, and probed at 500 nm using the time-correlated single photon counting method.

Charge carrier dynamics

Time-resolved photoluminescence (Tr-PL) analysis was performed to investigate the radiative recombination dynamics of electron–hole pairs bound by Coulomb interactions (Fig. 3). The Tr-PL measurements were carried out using a polymer in

© 2026 The Author(s). Published by the Royal Society of Chemistry

Open Access Article. Published on 07 August 2025. Downloaded on 1/18/2026 3:15:49 PM.
This article is licensed under a Creative Commons Attribution-NonCommercial 3.0 Unported Licence.

the TEA:MeOH:H_2O solution, ensuring consistent UV-vis absorbance across all samples. To account for both the fast initial decay and the slower tail dynamics observed in the Tr-PL decay curve, a bi-exponential equation was employed for fitting. The PL decay curves fitted with this model and the corresponding lifetimes are presented (Fig. S32 and Table S3). Due to low PL intensity, **PBT** and **PBT-F** were excluded from these measurements because the reliability of their Tr-PL signals was compromised. In **PBTzH-F**, a shorter exciton lifetime was observed, likely attributed to the added N atom that enhanced the molecular planarity and accelerated exciton dissociation into charge carriers. However, the increase in the number of EG groups in a side chain further extended the exciton lifetime by improving the polymer–solvent interactions, leading to increased PL intensity and enhanced exciton stabilization. This extended lifetime suggests that the EG groups stabilize excitons, thereby reducing the rate of radiative recombination and facilitating exciton diffusion and dissociation. This improved exciton lifetime, along with enhanced generation efficiency, is expected to enhance charge transfer and lead to higher hydrogen evolution efficiency. These results highlight the significance of side-chain engineering in extending exciton lifetime achieving a balance between radiative and non-radiative recombination processes, and ultimately improving the performance of photocatalysts in hydrogen evolution.

To investigate the charge separation and transfer dynamics, as well as non-radiative transitions, in the photoexcited state, transient absorption spectroscopy (TAS) measurements were conducted (Fig. 4) in TEA:MeOH:H_2O. In Fig. 4a, for **PBT**, there is a ground state bleach (GSB) signal at approximately 450 nm that decreases over time, while a photo-induced absorption (PIA) feature is observed beyond 600 nm. These signals likely originate from a combination of excitonic and polaronic species, which coexist and contribute simultaneously to the transient spectral response. The introduction of F substituents results in a noticeable blue shift in both the GSB and PIA peaks, along with an enhancement in the PIA signal, indicating more efficient charge generation in **PBT-F** compared to **PBT** (Fig. 4b). However, the relatively low exciton population observed in the PL spectra indicates limited availability of photogenerated electrons. This limitation not only constrains the overall hydrogen evolution efficiency but also, together with the prolonged lifetime of charge carriers, reflects inefficient hole transfer to the sacrificial agent, TEA, implying suboptimal charge separation dynamics. Fig. 4c shows that the transient absorption (TA) spectra exhibit a rapid decay of the GSB signal. Notably, a prominent PIA feature emerges around 450 nm at a delay time of 6 ns, followed by a sharp decay and the appearance of a long-lived PIA signal. This behavior is consistent with fast charge separation and subsequent charge accumulation, in agreement with the Tr-PL decay results. In Fig. 4d–f, the overall intensity of the TA signal decreases. For **3EG-PBTz-F** and **4EG-PBTz-F**, a PIA signal emerges at approximately 475 nm within the first 100 ns, displaying similar dynamics to those observed in **PBTzH-F**. Notably, the initial signal intensity increases with the length of the EG side chains, suggesting improved exciton dissociation at early times. Beyond 100 ns, the PIA peak undergoes a rapid spectral shift, accompanied by the appearance of a weak PIA feature around 550 nm. This evolution is indicative of the prompt transfer of photogenerated

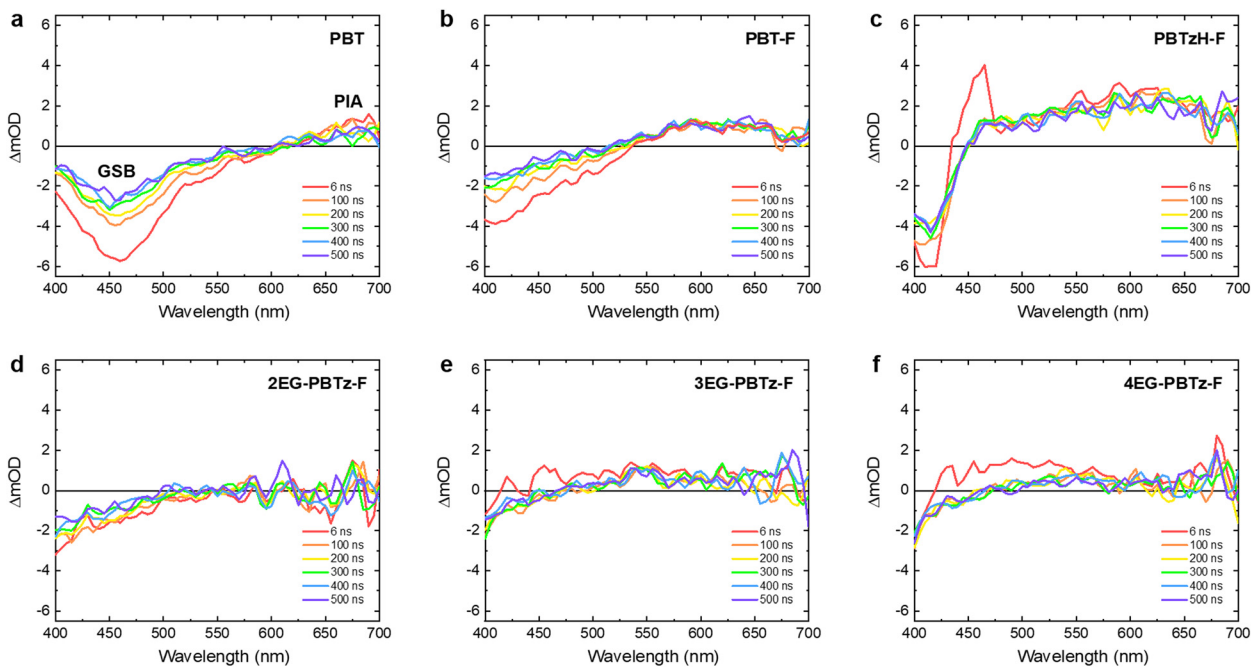

Fig. 4 Transient absorption (TA) spectra of the polymer nanoparticle dispersion of (a) **PBT**, (b) **PBT-F**, (c) **PBTzH-F**, (d) **2EG-PBTz-F**, (e) **3EG-PBTz-F**, and (f) **4EG-PBTz-F**. All polymers were dispersed in the same volume ratio of TEA:MeOH:H_2O and measured at various nanosecond timescale delays with 355 nm excitation (2 mJ cm^{-2}).

Open Access Article. Published on 07 August 2025. Downloaded on 1/18/2026 3:15:49 PM.
This article is licensed under a Creative Commons Attribution-NonCommercial 3.0 Unported Licence.

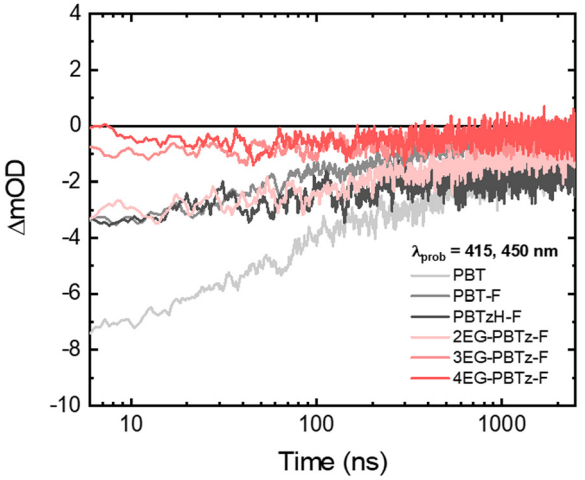

Fig. 5 TA kinetics of polymer particle dispersion. All polymers were dispersed in the same volume ratio of TEA:MeOH:H_2O and probed at 415 or 450 nm.

charged to TEA, implying that longer EG side chains facilitate strong polymer–solvent interactions, thereby suppressing exciton recombination and accelerating charge separation. Consequently, charge transfer efficiency is enhanced. Additionally, when focusing the TA measurement timescale to 100 ns, all polymer series exhibit quantitively similar dynamics to those observed in Fig. 4, although the overall signal intensity is increased. This indicates that charge separation and transfer occur on a sub-20 ns timescale. These short timescale measurements complement the long-time dynamics and further support the conclusion that charge separation in these materials is both efficient and rapid after excitation (Fig. S33).

To further investigate the charge transfer kinetics, we measured TA kinetics to track the time-dependent behavior of photoexcited electrons (Fig. 5). The lifetime obtained from biexponential fitting is also presented (Table S4). The longest charge lifetime was observed in **PBT**, indicating that excitons persist for an extended period after excitation but undergo slow non-radiative recombination without charge separation, as shown in Fig. 4a. The shorter lifetime in **PBT-F** and **PBTzH-F** is attributed to faster charge separation, as confirmed by the PIA signal in the TA spectra (Fig. 4b and c). In **PBT-F**, however, the PL data showed limited exciton generation, resulting in insufficient electron availability for hydrogen evolution despite efficient charge separation. Polymers with the EG groups exhibited faster charge lifetimes. Despite the short charge lifetime, the prolonged exciton lifetime observed in Tr-PL, along with a strong PIA signal at 6 ns, suggests stable excitons with slower recombination and rapid charge transfer following charge separation. This highlights efficient charge transfer, suggesting potential for improved hydrogen evolution efficiency.

Morphology and hydrophilicity

Liquid-phase transmission electron microscopy (LP-TEM) was used to analyze the size and morphology of polymer particles in a TEA:MeOH:H_2O solvent with an equal volume ratio (Fig. 6a). With the exception of **PBT-F**, particles were detected at a length scale of 50 nm. Spherical particles with radii ranging from approximately 25 to 50 nm were observed in polymer particles containing EG groups, suggesting a consistent morphology and adequately small particle sizes. Small, uniform particles demonstrate an enhanced specific surface area, offering more active sites for catalytic reactions.

The water contact angles were measured to evaluate the hydrophilicity of the polymers (Fig. 6b). The water contact angles for **PBT**, **PBT-F**, **PBTzH-F**, **2EG-PBTz-F**, **3EG-PBTz-F**, and **4EG-PBTz-F** were 64°, 61°, 64°, 52°, 42°, and 39°, respectively. The lowest contact angle, observed in **4EG-PBTz-F**, indicates a high degree of hydrophilicity, suggesting significant interaction between the polymer and water-rich environments. This characteristic promotes water molecule uptake on the polymer surface, thereby influencing charge transfer.

For a detailed analysis of the particle morphology at the nanoscale, small-angle X-ray scattering (SAXS) measurements were performed for each polymer in the TEA:MeOH:H_2O solution with an identical volume ratio.[54] In the low-q scattering region ($q < 0.02$ Å^{-1}), **4EG-PBTz-F** demonstrates the lowest power law exponent of −1.9, indicating a relatively loosely aggregated particle arrangement (Fig. 6c).[54–58] This loose arrangement leads to an increased surface area, facilitating water penetration into the polymer structure. This phenomenon is attributed to the presence of EG groups, which enhance polymer–solution interactions and promote efficient charge transfer pathways. Furthermore, the calculated radius of gyration (R_g) of **4EG-PBTz-F** from Guinier plot analysis was approximately 170 Å, suggesting a larger particle size and a loosely packed structure due to enhanced water penetration. This finding further supports the formation of electrons required for hydrogen evolution (Fig. S34).

Hydrogen evolution performance

Before evaluating the hydrogen evolution performance, it was necessary to optimize the polymer loading in the reaction solution. The experiment was conducted by varying the polymer amount to 0.5, 1.0, 1.5, and 2.0 mg (Fig. S35). A significant increase in hydrogen evolution was observed at 1.5 mg, while a decrease was recorded at 2.0 mg. At this higher loading, precipitation of polymer particles occurred, likely due to the excessive amount. Based on these results, 1.5 mg was selected as the optimal polymer loading. Subsequently, the photocatalytic efficiency of all polymer photocatalysts was assessed under artificial solar irradiation (Xenon lamp, 100 mW cm^{-2}) with TEA as a hole scavenger, using a TEA : MeOH : H_2O (1 : 1 : 1, 0.5 mg mL^{-1}) solution containing 1.5 mg of polymer. Hydrogen evolution was quantified using gas chromatography with a gas-tight syringe. An image of the polymer dispersion for hydrogen evolution performance is also provided (Fig. S36).

As shown in Fig. 7a and b, **4EG-PBTz-F** achieved the highest HER of 15.476 mmol g^{-1} and 3.095 mmol g^{-1} h^{-1} with 3 wt% Pt, representing an approximately five-fold increase compared to **PBT**. This significant improvement in hydrogen evolution is

© 2026 The Author(s). Published by the Royal Society of Chemistry

Open Access Article. Published on 07 August 2025. Downloaded on 1/18/2026 3:15:49 PM.
This article is licensed under a Creative Commons Attribution-NonCommercial 3.0 Unported Licence.

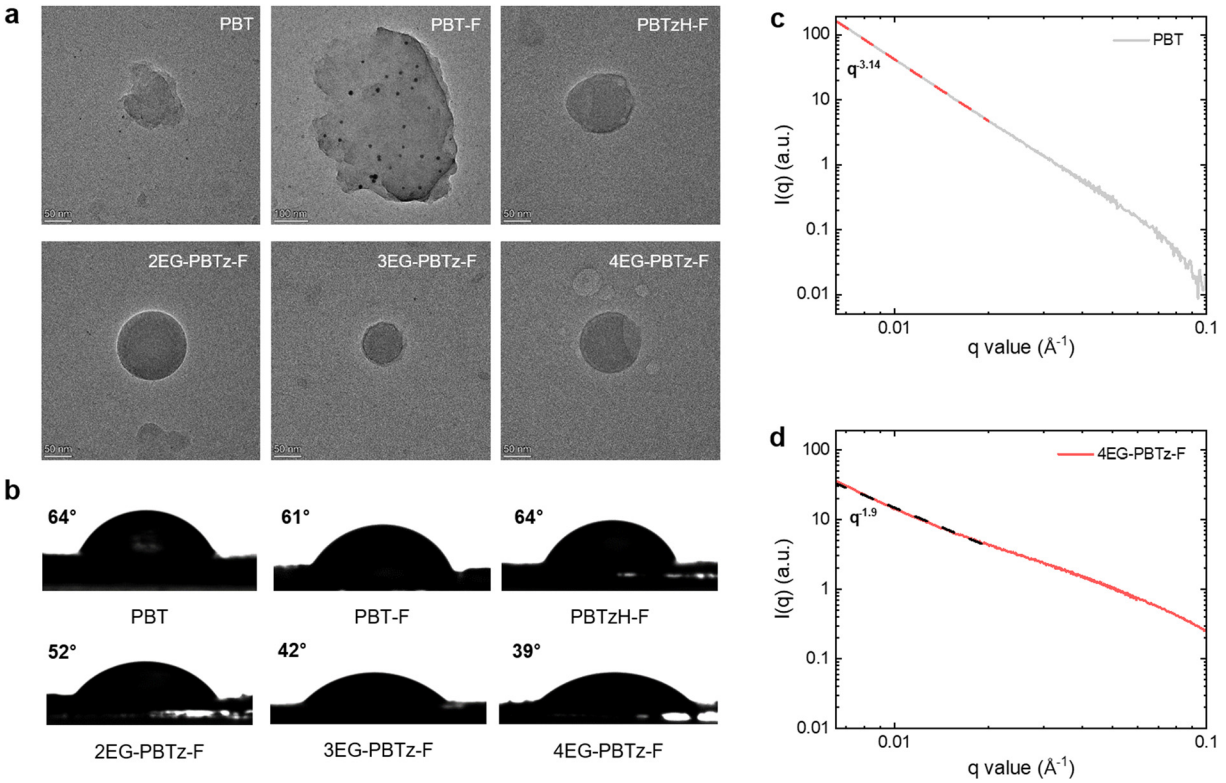

Fig. 6 Morphology and hydrophilicity measurements of the polymers. (a) Transmission electron microscopy (TEM) image of polymer dispersion in the same volume ratio of TEA:MeOH:H_2O. (b) Water contact angle of the polymers in pellets. Small-angle X-ray scattering (SAXS) profiles of (c) **PBT** and (d) **4EG-PBTz-F** obtained from the polymer dispersions prepared in a TEA:MeOH:H_2O solvent with the same volume ratio.

attributed to the incorporation of F substituents and EG side chains, which enhance the polarity of the polymer, facilitating interaction with water. The improved polarity facilitates water absorption and enhances exciton generation, charge separation, and hydrogen evolution. Optical analyses confirmed the positive impact of side-chain engineering on photocatalytic performance. Moreover, increasing the number of EG side chains further enhanced hydrogen evolution, likely due to increased solvent interaction resulting from enhanced hydrophilicity. Interestingly, **PBTzH-F** outperformed **2EG-PBTz-F** and **3EG-PBTz-F** in terms of hydrogen evolution, which can be in explained by its superior dispersion in the solvent, enabling enhanced water penetration and performance.

To evaluate the photocatalytic efficiency of **4EG-PBTz-F**, measurements were taken for the apparent quantum yield (AQY) and photocatalytic stability (Fig. 7c and d). The AQY values were determined as 0.78% at 400 nm, 0.49% at 420 nm, 0.20% at 450 nm, and 0.14% at 500 nm, which aligns with its UV absorption spectrum, suggesting an enhancement in hydrogen evolution efficiency with increased light absorption. The photocatalytic stability of **4EG-PBTz-F** was examined over a 15-hour period, divided into three 5-hour cycles. Following each reaction period, the catalyst was recovered through centrifugation, and a fresh hole scavenger solution was then added to prepare the system for subsequent measurements. The photocatalytic performance remained consistent across all cycles, with the second cycle demonstrating higher hydrogen evolution compared to the first cycle. These findings confirm the stability and reproducibility of **4EG-PBTz-F** for sustainable photocatalytic applications. Furthermore, the effect of hole scavengers on hydrogen evolution was investigated using three different scavengers, with Pd residue from polymer synthesis as the only co-catalyst. As shown in Fig. S37a and S37b, TEA exhibited the highest hydrogen evolution performance, likely due to its superior dispersibility within the system.

Conclusions

In conclusion, a dual-electron-acceptor copolymer, **PBT**, was successfully synthesized by combining DBS and BT units to enhance electron-withdrawing capability and maximize electron output sites. The subsequent incorporation of di-fluoro substituents and EG groups into the BT unit improved molecular planarity and strengthened interactions between the polymer and aqueous environment. The photocatalytic hydrogen evolution mechanism was determined through time-resolved optical analyses and charge carrier dynamics, revealing key processes from exciton generation to charge separation, transport, and eventual hydrogen evolution. Furthermore, Tr-PL and TAS measurements exhibited that the incorporation of side chains effectively suppressed exciton recombination and accelerated charge separation and transfer within the electron–hole pair, thereby facilitating efficient hydrogen evolution.

Open Access Article. Published on 07 August 2025. Downloaded on 1/18/2026 3:15:49 PM. This article is licensed under a Creative Commons Attribution-NonCommercial 3.0 Unported Licence.

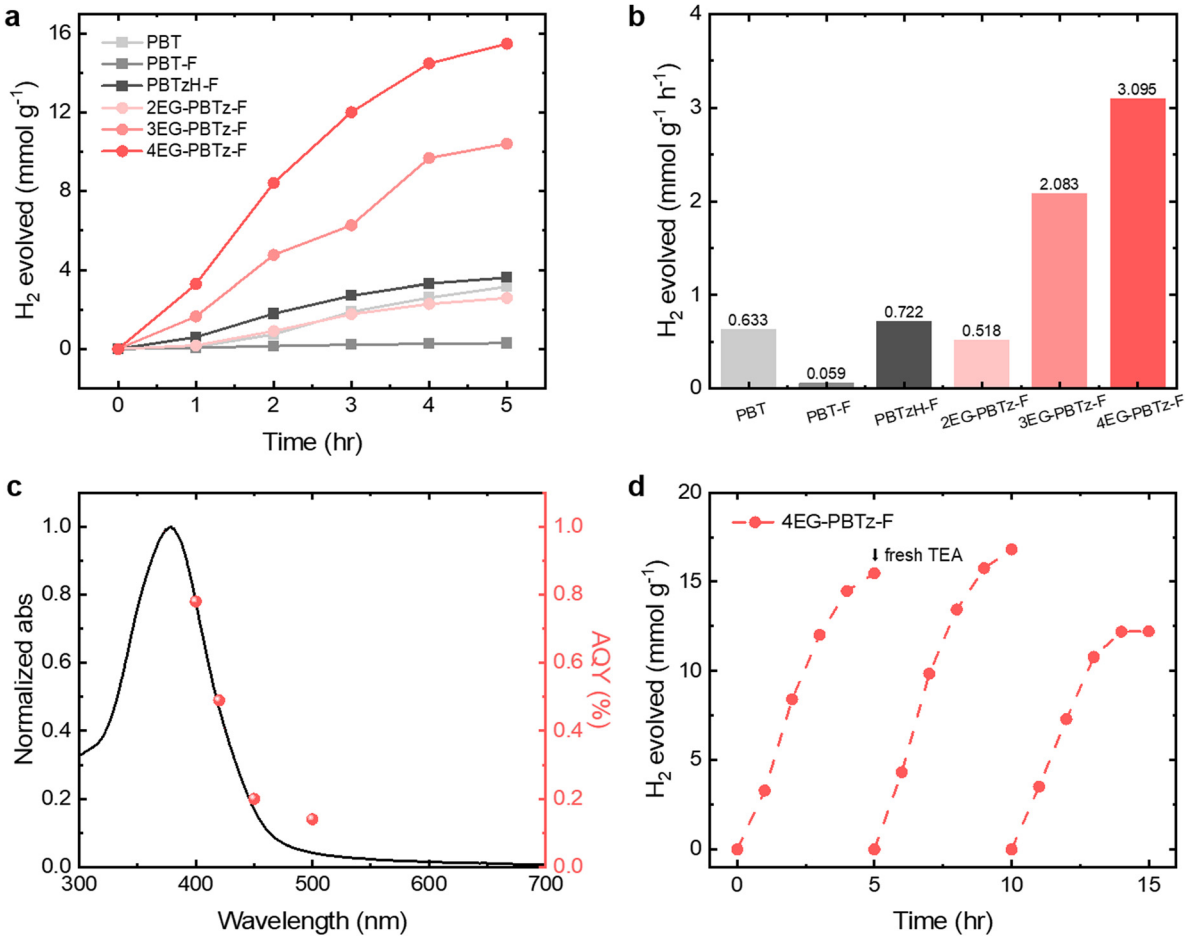

Fig. 7 Hydrogen evolution experiments of the polymers. (a) Hydrogen evolution rate (HER) over time, (b) total hydrogen evolution, (c) apparent quantum yield (AQY) of **4EG-PBTz-F** at 400 nm, 420 nm, 450 nm, and 500 nm, and (d) photocatalytic stability of **4EG-PBTz-F** over 15 h in three cycles of 5 h. All experiments, excluding the AQY measurements, were performed using reaction solutions comprising 1.5 mg of polymer (0.5 mg mL^{-1}) in a TEA:MeOH:H_2O solvent with a fixed volume ratio. The AQY measurements for hydrogen evolution were conducted using reaction solutions containing 3 mg of polymer (1 mg mL^{-1}) in a TEA:MeOH:H_2O solution with a fixed volume ratio.

Moreover, contact angle measurements and SAXS analysis revealed that EG groups promoted water penetration into the polymer, enhancing hydrophilicity and dispersibility. As a result, **4EG-PBTz-F**, which incorporates di-fluoro substituents and tetra-ethylene glycol groups, achieved an HER of 3.095 mmol g^{-1} h^{-1}, approximately five times higher than that of **PBT**. This study therefore highlights the potential of dual-acceptor systems in photocatalysis and demonstrates side-chain engineering as a viable strategy for enhancing hydrogen evolution efficiency.

Author contributions

S. Kim: conceptualization, data curation, formal analysis, investigation, validation, visualization, and writing – original draft; Y. Yu: conceptualization, data curation, formal analysis, investigation, resources, validation, visualization and writing – original draft; H. Choi: investigation and resources; G. Ham: investigation and visualization; S. An: resources; S. Lee: data curation and investigation; J. Yang: data curation; D. S. Chung: resources; J. Lee: conceptualization, formal analysis, funding acquisition, project administration, resources, supervision and writing – review & editing; H. Cha: conceptualization, funding acquisition, project administration, resources, supervision and writing – review & editing.

Conflicts of interest

There are no conflicts to declare.

Data availability

The data supporting this article have been included as part of the SI.

Synthetic details, polymer characterization data, PXRD data, TGA data, DFT calculation, Tauc plot, TAS data, SAXS data, images of polymer dispersion, hydrogen evolution experiments, ICP-OES data and Tr-PL data. See DOI: **https://doi.org/10.1039/d5ey00155b**.

© 2026 The Author(s). Published by the Royal Society of Chemistry

Open Access Article. Published on 07 August 2025. Downloaded on 1/18/2026 3:15:49 PM. This article is licensed under a Creative Commons Attribution-NonCommercial 3.0 Unported Licence.

Acknowledgements

This work was supported by the National Research Foundation of Korea (RS-2023-00213920 and RS-2024-00438426). This research was supported by the Basic Science Research Program through the National Research Foundation of Korea (NRF) funded by the Ministry of Education (2018R1A6A1A03023788). This work was also supported by Chungcheongbuk-do RISE (Regional Innovation System & Education) grants funded by the Ministry of Education and Chungcheongbuk-do.

References

1 C. Bauer, K. Treyer, C. Antonini, J. Bergerson, M. Gazzani, E. Gencer, J. Gibbins, M. Mazzotti, S. T. McCoy, R. McKenna, R. Pietzcker, A. P. Ravikumar, M. C. Romano, F. Ueckerdt, J. Ventek and M. van der Spek, *Sustainable Energy Fuels*, 2022, **6**, 66–75.
2 V. A. Panchenko, Y. V. Daus, A. A. Kovalev, I. V. Yudaev and Y. V. Litti, *Int. J. Hydrogen Energy*, 2023, **48**, 4551–4571.
3 J. Jia, L. C. Seitz, J. D. Benck, Y. Huo, Y. Chen, J. W. D. Ng, T. Bilir, J. S. Harris and T. F. Jaramillo, *Nat. Commun.*, 2016, **7**, 13237.
4 A. Landman, H. Dotan, G. E. Shter, M. Wullenkord, A. Houaijia, A. Maljusch, G. S. Grader and A. Rothschild, *Nat. Mater.*, 2017, **16**, 646–651.
5 T. Takata, J. Jiang, Y. Sakata, M. Nakabayashi, N. Shibata, V. Nandal, K. Seki, T. Hisatomi and K. Domen, *Nature*, 2020, **581**, 411–414.
6 B. D. Fath, *Managing Air Quality and Energy Systems*, CRC Press, Boca Raton, FL, USA, 2nd edn, 2020.
7 Z. Yu, K. Yan, W. Ullah, H. Chen and C. Li, *ACS Appl. Polym. Mater.*, 2021, **3**, 60–92.
8 A. Fujishima and K. Honda, *Nature*, 1972, **238**, 37–38.
9 Y. Pihosh, I. Turkevych, K. Mawatari, J. Uemura, Y. Kazoe, S. Kosar, K. Makita, T. Sugaya, T. Matsui, D. Fujita, M. Tosa, M. Kondo and T. Kitamori, *Sci. Rep.*, 2015, **5**, 11141.
10 X. Zhang, Y. Zhou, D. Wu, X. Liu, R. Zhang, H. Liu, C. Dong, J. Yang, S. A. Kulinich and X. Du, *J. Mater. Chem. A*, 2018, **6**, 9057–9063.
11 J. R. Darwent and G. Porter, *J. Chem. Soc., Chem. Commun.*, 1981, 145–146.
12 W. Zhao, Q. Zhao, Z. Song, L. Ma, X. Chen, S. Ding and L. Zhou, *ACS Appl. Nano Mater.*, 2022, **5**, 16440–16450.
13 X. Wang, K. Maeda, A. Thomas, K. Takanabe, G. Xin, J. M. Carlsson, K. Domen and M. Antonietti, *Nat. Mater.*, 2008, **8**, 76–80.
14 X. Wang, L. Chen, S. Y. Chong, M. A. Little, Y. Wu, W. Zhu, R. Clowes, Y. Yan, M. A. Zwijnenburg, R. S. Sprick and A. I. Cooper, *Nat. Chem.*, 2018, **10**, 1180–1189.
15 F. Zhang, J. Sheng, Z. Yang, X. Sun, H. Tang, M. Lu, H. Dong, F. Shen, J. Liu and Y. Lan, *Angew. Chem.*, 2018, **6**, 1212–1218.
16 L. Wang, R. Fernández-Terán, L. Zhang, D. L. A. Fernandes, L. Tian, H. Chen and H. Tian, *Angew. Chem., Int. Ed.*, 2016, **55**, 12306.
17 J. Kosco, M. Bidwell, H. Cha, T. Martin, C. T. Howells, M. Sachs, D. H. Anjum, S. Gonzalez Lopez, L. Zou, A. Wadsworth, W. Zhang, L. Zhang, J. Tellam, R. Sougrat, F. Laquai, D. M. DeLongchamp, J. R. Durrant and I. McCulloch, *Nat. Mater.*, 2020, **19**, 559–565.
18 M. Sachs, R. S. Sprick, D. Pearce, S. A. J. Hillman, A. Monti, A. A. Y. Guilbert, N. J. Brownbill, S. Dimitrov, X. Shi, F. Blanc, M. A. Zwijnenburg, J. Nelson, J. R. Durrant and A. I. Cooper, *Nat. Commun.*, 2018, **9**, 4968.
19 J. Kosco, S. Gonzalez-Carrero, C. T. Howells, W. Zhang, M. Moser, R. Sheelamanthula, L. Zhao, B. Willner, T. C. Hidalgo, H. Faber, B. Purushothaman, M. Sachs, H. Cha, R. Sougrat, T. D. Anthopoulos, S. Inal, J. R. Durrant and I. McCulloch, *Adv. Mater.*, 2022, **34**, 2105007.
20 H. H. Cho, L. Yao, J. H. Yum, Y. Liu, F. Boudoire, R. A. Wells, N. Guijarro, A. Sekar and K. Sivula, *Nat. Catal.*, 2021, **4**, 431–438.
21 A. Brnovic, L. Hammarström and H. Tian, *J. Phys. Chem. C*, 2023, **127**, 12631–12639.
22 S. Yanagida, A. Kabumoto, K. Mizumoto, C. Pac and K. Yoshino, *J. Chem. Soc., Chem. Commun.*, 1985, 474–475.
23 G. Zhang, Z. Lan and X. Wang, *Angew. Chem., Int. Ed.*, 2016, **55**, 15712.
24 C. Zhao, Z. Chen, R. Shi, X. Yang and T. Zhang, *Adv. Mater.*, 2020, **32**, 1907296.
25 S. A. J. Hillman, R. S. Sprick, D. Pearce, D. J. Woods, W. Sit, X. Shi, A. I. Cooper, J. R. Durrant and J. Nelson, *J. Am. Chem. Soc.*, 2022, **144**, 19382–19395.
26 H. Zhao, Y. Dong, P. Sun, Y. Bai, C. Ru, X. Wu, Z. Li, X. Han, J. Wu and X. Pan, *ACS Appl. Energy Mater.*, 2022, **5**, 4631–4640.
27 Y. Su, K. Li, Z. Li, Y. Tian, B. Liu, G. Yue and Y. Tian, *J. Colloid Interface Sci.*, 2024, **661**, 333–344.
28 W. Lin, J. Jayakumar, C. Chang, L. Ting, T. Huang, M. H. Elsayed, A. M. Elewa, Y. Lin, J. Liu, Y. Tseng and H. Chou, *J. Mater. Chem. A*, 2022, **10**, 6641–6648.
29 M. Axelsson, C. F. N. Marchiori, P. Huang, C. M. Araujo and H. Tian, *J. Am. Chem. Soc.*, 2021, **143**, 21229–21233.
30 Y. Xiang, X. Wang, L. Rao, P. Wang, D. Huang, X. Ding, X. Zhang, S. Wang, H. Chen and Y. Zhu, *ACS Energy Lett.*, 2018, **3**, 2544–2549.
31 C. Chang, W. Lin, L. Ting, C. Shih, S. Chen, T. Huang, H. Tateno, J. Jayakumar, W. Jao, C. Tai, C. Chu, C. Chen, C. Yu, Y. Lu, C. Hu, A. M. Elewa, T. Mochizuki and H. Chou, *Nat. Commun.*, 2022, **13**, 5460.
32 T. Huang, J. Liu, Z. Lai, J. Chang, Y. Zhuang, Z. Jiang, C. Chang, W. Lin, Y. Chen, Y. Wu, Y. Sun, T. Luo, Y. Chen, J. Yen, H. Hsu, B. Chen, L. Ting, C. Lu, Y. Lin, L. Hsu, T. Wu, S. Yang, A. Su, U. Jeng and H. Chou, *Small*, 2024, **20**, 2304743.
33 Y. Jo, J. G. Oh, C. Kim, T. K. An, J. Jang and J. Lee, *J. Ind. Eng. Chem.*, 2020, **86**, 150–157.
34 S. E. Tan and M. S. Sarjadi, *Malays. J. Fundam. Appl. Sci.*, 2017, **13**, 760–763.
35 U. Salma and Y. Nagao, *Polym. Degrad. Stab.*, 2020, **179**, 109299.

© 2026 The Author(s). Published by the Royal Society of Chemistry

Open Access Article. Published on 07 August 2025. Downloaded on 1/18/2026 3:15:49 PM.
This article is licensed under a Creative Commons Attribution-NonCommercial 3.0 Unported Licence.

36 C. M. Aitchison, R. S. Sprick and A. I. Cooper, *J. Mater. Chem. A*, 2019, **7**, 2490–2496.
37 C. Cheng, X. Wang, Y. Lin, L. He, J. Jiang, Y. Xu and F. Wang, *Polym. Chem.*, 2018, **9**, 4468–4475.
38 C. Dai, S. Xu, W. Liu, X. Gong, M. Panahandeh-Fard, Z. Liu and B. Liu, *Small*, 2018, **14**, 1801839.
39 C. Han, S. Xiang, S. Jin, L. Luo, C. Zhang, C. Yan and J. Jiang, *J. Mater. Chem. A*, 2022, **10**, 5255–5261.
40 S. Jin, C. Han, S. Xiang, C. Zhang and J. Jiang, *J. Catal.*, 2023, **427**, 115091.
41 Z. Li, F. Zhao, Y. Chu, F. Meng, Y. Dong, H. Zhang and S. Wang, *ACS Sustain. Chem. Eng.*, 2023, **12**, 1072–1083.
42 R. Li, X. Zhang, C. Zhang, J. Lu, J. Wang, C. Cui and Y. Zhang, *Int. J. Hydrogen Energy*, 2022, **47**, 29771–29780.
43 Z. Tan, Y. Xing, J. Cheng, G. Zhang, Z. Shen, Y. Zhang and S. Liu, *Chem. Sci.*, 2022, **13**, 1725–1733.
44 X. Yuan, K. Yang, C. Grazon, C. Wang, L. Vallan, J. Isasa, P. M. Resende, F. Li, C. Brochon, H. Remita, G. Hadziioannou, E. Cloutet and J. Li, *Angew. Chem., Int. Ed.*, 2024, **136**, e202315333.
45 J. Kosco, M. Sachs, R. Godin, M. Kirkus, L. Francas, M. Bidwell and I. McCulloch, *Adv. Energy Mater.*, 2018, **8**, 1802181.
46 D. J. Woods, S. A. Hillman, D. Pearce, L. Wilbraham, L. Q. Flagg, W. Duffy and M. A. Zwijnenburg, *Energy Environ. Sci.*, 2020, **13**, 1843–1855.
47 M. Yu, W. Zhang, Z. Guo, Y. Wu and W. Zhu, *Angew. Chem., Int. Ed.*, 2021, **60**, 15590–15597.
48 S. An, Z. Wu, H. Jeong, J. Lee, S. Y. Jeong, W. Lee, S. Kim, J. W. Han, J. Lim, H. Cha, H. Y. Woo and D. S. Chung, *Small*, 2023, **19**, 2204905.
49 X. Yuan, C. Wang, L. Vallan, A. T. Bui, G. Jonusauskas, N. D. McClenaghan, C. Grazon, S. Lacomme, C. Brochon, H. Remita, G. Hadziioannou and E. Cloutet, *Adv. Funct. Mater.*, 2023, **33**, 2211730.
50 L. Ting, J. Jayakumar, C. Chang, W. Lin, M. H. Elsayed and H. Chou, *J. Mater. Chem. A*, 2019, **7**, 22924–22929.
51 W. Lin, J. Jayakumar, C. Chang, L. Ting, M. H. Elsayed, M. Abdellah, K. Zheng, A. M. Elewa, Y. Lin, J. Liu, W. Wang, C. Lu and H. Chou, *Appl. Catal., B*, 2021, **298**, 120577.
52 C. Han, S. Xiang, P. Xie, P. Dong, C. Shu, C. Zhang and J. X. Jiang, *Adv. Funct. Mater.*, 2022, **32**, 2109423.
53 R. J. Lyons, Y. Yang, E. McQueen, L. Luo, A. I. Cooper, M. A. Zwijnenburg and R. S. Sprick, *Adv. Energy Mater.*, 2024, **14**, 2303680.
54 K. Kim, J. Kim, Y. D. Yun, H. Ahn, B. Min, N. H. Kim, S. Rah, H. Kim, C. Lee, I. D. Seo, W. Lee, H. J. Choi and K. S. Jin, *Biodesign*, 2017, **5**, 24–29.
55 S. Zhao, S.-S. Shen, L. Han, B.-C. Tian, N. Li, W. Chen and X.-B. Li, *Rare Met.*, 2024, **43**, 4038–4055.
56 X. Li, Q. Liu, F. Deng, J. Huang, L. Han, C. He, Z. Chen, Y. Luo and Y. Zhu, *Appl. Catal., B*, 2022, **314**, 121502.
57 X. Li, T. Han, Y. Zhou, Y. Xie, Y. Luo, J. Huang, Z. Chen and F. Deng, *Sci. China: Technol. Sci.*, 2024, **67**, 1238–1252.
58 S. Shen, X. Li, Y. Zhou, L. Han, Y. Xie, F. Deng, J. Huang, Z. Chen, Z. Feng, J. Xu and F. Dong, *J. Mater. Sci. Technol.*, 2023, **155**, 148–159.

© 2026 The Author(s). Published by the Royal Society of Chemistry